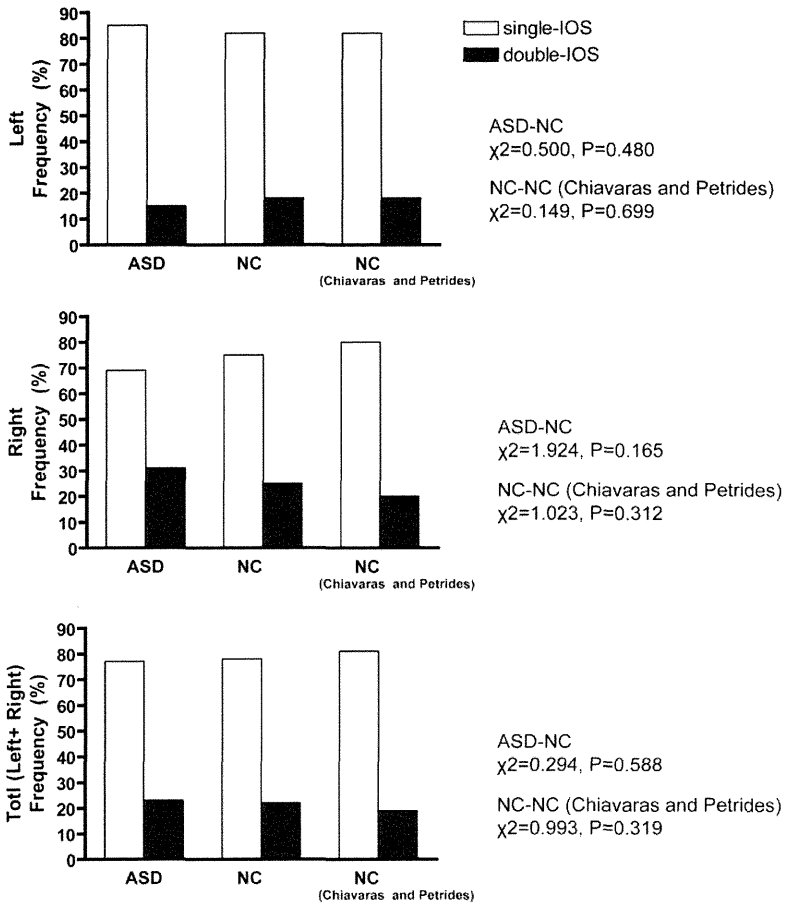

Fig. 4 Sulcal pattern distribution of the IOS in the OFC. Right column shows results from Chiavaras and Petrides (2000). No significant distribution difference was found between groups.

Table 3 Categorical regression analysis

Clinical/cognitive measures (dependent variables)	ASD group					NC group				
	ANOVA	Independent variables	β	F	P	ANOVA	Independent variables	β	F	P
AQ										
Total score	**$F(6,47) = 2.689$, $P = 0.027$**	**Type I**	**−0.479**	**8.139**	**0.007**	$F(6,42) = 0.491$, $P = 0.811$	Type I	0.043	0.055	0.816
		Type II	**−0.334**	**4.228**	**0.046**		Type II	0.052	0.072	0.790
		Type III	0.084	0.245	0.623		Type III	0.105	0.361	0.552
		Absent POS	−0.163	1.017	0.319		Absent POS	−0.163	0.759	0.389
		Single POS	0.276	3.344	0.075		Single POS	0.097	0.220	0.642
		Double POS	0.131	0.799	0.377		Double POS	0.021	0.011	0.918
Social interaction	$F(6,47) = 1.680$, $P = 0.150$	Type I	0.173	0.945	0.337	$F(6,42) = 1.907$, $P = 0.106$	Type I	0.306	3.379	0.074
		Type II	−0.396	5.335	0.026		Type II	−0.004	0.001	0.982
		Type III	−0.159	0.780	0.382		Type III	0.242	2.321	0.136
		Absent POS	−0.321	3.501	0.068		Absent POS	−0.315	.3471	0.071
		Single POS	−0.153	0.916	0.344		Single POS	0.185	0.972	0.331
		Double POS	0.276	3.191	0.081		Double POS	0.156	0.699	0.409
Attention to detail	**$F(6,47) = 2.909$, $P = 0.019$**	**Type I**	**−0.420**	**6.399**	**0.015**	$F(6,42) = 1.735$, $P = 0.141$	Type I	−0.182	1.168	0.287
		Type II	−0.101	0.399	0.531		Type II	0.048	0.071	0.792
		Type III	0.023	0.019	0.890		Type III	−0.085	0.278	0.601
		Absent POS	0.097	0.367	0.548		Absent POS	0.320	3.507	0.069
		Single POS	−0.217	2.103	0.155		Single POS	−0.190	1.008	0.322
		Double POS	0.112	0.602	0.442		Double POS	−0.108	0.326	0.571

Bold fonts represent statistically significant effects.

neurodevelopmental studies of infant brains together with our findings of altered sulcogyral morphology may provide new insight into critical gestation periods during which abnormal developmental processes lead to the altered sulcogyral formation in ASD (Bachevalier and Loveland, 2006).

We also found an interesting ASD case in which the rostral parts of the OFC were extremely small in both hemispheres and therefore could not be classified into any of the known variations of the orbitofrontal sulcogyral pattern. It is of note that this individual is highly intelligent with markedly successful academic achievements. Given the observation that expression of Type III, the least common pattern in a neurotypical population, was increased in the ASD group, this case could be interpreted as an extreme case of underdevelopment of the orbitofrontal sulcogyral formation. Therefore, this ASD case also suggests the possible link between abnormal orbitofrontal sulcogyral formation and the etiology of ASD.

Commonality and differences between ASD and schizophrenia

Increased Type III and decreased Type I expressions have been previously demonstrated in the right hemisphere of schizophrenic individuals, replicated by at least three different institutes (Nakamura *et al.*, 2007; Chakirova *et al.*, 2010; Takayanagi *et al.*, 2010). Converging findings from first-episode schizophrenia and individuals with high risk of developing schizophrenia indicated that the presence of Type III in the right hemisphere may be a trait marker for developing psychotic symptoms in schizophrenia (Nakamura *et al.*, 2007; Chakirova *et al.*, 2010). The same pattern of increased Type III coupled with decreased Type I in the right hemisphere was also identified in our study of ASD. Our finding of a shared morphological feature between ASD and schizophrenia is consistent with that of previous studies emphasizing overlaps between the two diseases at multiple levels, including clinical symptoms (Urfer-Parnas *et al.*, 2010; Parnas, 2011), social cognition (Solomon *et al.*, 2011), brain activity (Sugranyes *et al.*, 2011), brain morphology (Cheung *et al.*, 2010) and gene mutations (Guilmatre *et al.*, 2009; Rapoport *et al.*, 2009). However, an important difference exists such that a significant alteration was found in both hemispheres in ASD, whereas the sulcal pattern was only altered in the right hemisphere in schizophrenia. Previous neuropsychological studies have shown that a bilateral lesion of the OFC causes more severe deficits in social and emotional functioning than does a unilateral lesion (Bramham *et al.*, 2009). Therefore, the manifestation of clear social and behavioral abnormalities characteristic to ASD may become more likely when neurodevelopmental abnormalities affect the OFC in both hemispheres.

Restricted and repetitive behaviors in ASD

Using categorical regression analysis for predicting specific ASD traits, we found that the presence of Type I is associated with a reduced score on the 'attention to detail' subscale. This result could be consistent with that of a previous study reporting that Type I expression was associated with milder clinical symptoms in male schizophrenia (Nakamura *et al.*, 2007). The factor of 'attention to detail' in the AQ test belongs to 'high-level' RRBs (Turner, 1999) characterized by an adherence to some rule or mental set leading to rigidity and inflexibility, and is also observed in individuals with obsessive–compulsive disorder (OCD) (Lewis and Kim, 2009). While previous neuroimaging studies of OCD have accumulated evidence for structural and functional abnormalities of the OFC (see reviews by Maia *et al.*, 2008 and Rotge *et al.*, 2009), involvement of the OFC for RRB has not been clearly demonstrated in ASD, although the implication of other structures has been suggested (e.g. striatum) (Sears *et al.*, 1999; Hollander *et al.*, 2005; Rojas *et al.*, 2006). Given our finding of altered distribution of orbitofrontal sulcogyral subtypes in ASD, it would be interesting in future studies to measure the gray matter volume and/or density in the OFC separately for each subtype and examine possible associations with behavioral measures as previously done for schizophrenia (Nakamura *et al.*, 2008).

Variations in POS and IOS patterns

We found evidence of increased cases of absent POS in the right hemisphere together with decreased cases of single POS in ASD, whereas no significant group difference was observed in the IOS pattern. The POS and IOS are located in the posterior and anterior OFC gyri, respectively. According to a model of OFC function, the posterior OFC houses multimodal representations for visual, auditory, somatosensory, gustatory and olfactory sensations that are then linked to particular reward value representations (Kringelbach and Rolls, 2004). Recently, abnormalities in sensory processing have been demonstrated in all five classic sensory modalities in ASD (Marco *et al.*, 2011), and altered reactivity to sensory inputs is now included as one of the new diagnostic criteria for ASD in DSM-V (Mandy *et al.*, 2012). It is possible that an underdeveloped sulcogyral pattern in the posterior orbitofrontal gyrus may be related to sensory abnormalities and unusual affections associated with sensations.

Limitations

We note several limitations in this study. First, except for the association between the autistic factor of 'attention to detail' and Type III expression in the right hemisphere, this study alone does not clearly demonstrate which functions are particularly affected by altered orbitofrontal sulcogyral patterns. Because the entire OFC is engaged in diverse functions, many of which are altered in ASD, future studies may need an extended neuropsychological test battery to examine the relationship between sulcogyral variations and altered functions more thoroughly. Second, we used the AQ for assessing the severity of autistic traits. Although the AQ is a validated self-report questionnaire (Baron-Cohen *et al.*, 2001; Wakabayashi *et al.*, 2006), it would be desirable to have other standard assessment procedures such as the Autism Diagnostic Interview Revised to support the evaluation of autistic traits in each individual. Third, our sample was limited to the male population. While the present approach is advantageous in terms of sample homogeneity, our analyses need to be applied to female patients as well given a recent finding of a significant dimorphic distribution of the H-shaped sulcus in schizophrenia (Uehara-Aoyama *et al.*, 2011). Finally, it remains unclear whether and how expressions of particular sulcogyral subtypes are associated with other structural measures, such as regional tissue density or volume in the OFC. Although our preliminary VBM analysis suggested increased white matter density in the OFC among ASD individuals with the double-POS type, small number of subjects of this subtype did not allow us to draw firm conclusions (see Supplementary material 2).

In conclusion, this study examined morphological variations of the multiple orbitofrontal sulci in ASD and revealed significant alterations in distributions of sulcal subtypes in the H-shaped sulcus in both hemispheres and the right POS. Furthermore, expressions of specific subtypes of the H-shaped sulcus were associated with the degree of general and specific autistic traits. These findings indicate that the altered orbitofrontal sulcogyral pattern may be used as a morphological trait marker that reflects abnormal neurodevelopmental processes leading to an elevated risk of developing autistic symptoms.

SUPPLEMENTARY DATA

Supplementary data are available at *SCAN* online.

Conflict of Interest

None declared.

REFERENCES

Armstrong, E., Schleicher, A., Omran, H., Curtis, M., Zilles, K. (1995). The ontogeny of human gyrification. *Cerebral Cortex, 5*(1), 56–63.

Bachevalier, J., Loveland, K.A. (2006). The orbitofrontal-amygdala circuit and self-regulation of social-emotional behavior in autism. *Neuroscience and Biobehavioral Reviews, 30*(1), 97–117.

Barbas, H., Pandya, D.N. (1989). Architecture and intrinsic connections of the prefrontal cortex in the rhesus monkey. *Journal of Comparative Neurology, 286*(3), 353–75.

Baron-Cohen, S. (2002). The extreme male brain theory of autism. *Trends in Cognitive Sciences, 6*(6), 248–54.

Baron-Cohen, S., Wheelwright, S., Skinner, R., Martin, J., Clubley, E. (2001). The autism-spectrum quotient (AQ): evidence from Asperger syndrome/high-functioning autism, males and females, scientists and mathematicians. *Journal of Autism and Developmental Disorders, 31*(1), 5–17.

Bartley, A.J., Jones, D.W., Weinberger, D.R. (1997). Genetic variability of human brain size and cortical gyral patterns. *Brain, 120*(Pt 2), 257–69.

Bramham, J., Morris, R.G., Hornak, R.G., Bullock, P., Polkey, C.E. (2009). Social and emotional functioning following bilateral and unilateral neurosurgical prefrontal cortex lesions. *Journal of Neuropsychology, 3*(Pt 1), 125–43.

Chakirova, G., Welch, K.A., Moorehead, T.W., et al. (2010). Orbitofrontal morphology in people at high risk of developing schizophrenia. *European Psychiatry, 25*(6), 366–72.

Cheung, C., Yu, K., Fung, G., et al. (2010). Autistic disorders and schizophrenia: related or remote? An anatomical likelihood estimation. *PLoS ONE, 5*(8), e12233.

Chi, J.G., Dooling, E.C. (1976). Gyral development of the human brain. *Transactions of the American Neurological Association, 101*, 89–90.

Chiavaras, M.M., Petrides, M. (2000). Orbitofrontal sulci of the human and macaque monkey brain. *Journal of Comparative Neurology, 422*(1), 35–54.

Dane, S., Balci, N. (2007). Handedness, eyedness and nasal cycle in children with autism. *International Journal of Developmental Neuroscience, 25*(4), 223–6.

Dubois, J., Benders, M., Cachia, A., et al. (2008). Mapping the early cortical folding process in the preterm newborn brain. *Cerebral Cortex, 18*(6), 1444–54.

Gillberg, C. (1983). Autistic children's hand preferences: results from an epidemiological study of infantile autism. *Psychiatry Research, 10*(1), 21–30.

Girgis, R.R., Minshew, N.J., Melhem, N.M., et al. (2007). Volumetric alterations of the orbitofrontal cortex in autism. *Progress in Neuropsychopharmacology and Biological Psychiatry, 31*(1), 41–5.

Guilmatre, A., Dubourg, C., Mosca, A.L., et al. (2009). Recurrent rearrangements in synaptic and neurodevelopmental genes and shared biologic pathways in schizophrenia, autism, and mental retardation. *Archives of General Psychiatry, 66*(9), 947–56.

Habas, P.A., Scott, J.A., Roosta, A., et al. (2012). Early folding patterns and asymmetries of the normal human brain detected from in utero MRI. *Cerebral Cortex, 22*(1), 13–25.

Hauck, J.A., Dewey, D. (2001). Hand preference and motor functioning in children with autism. *Journal of Autism and Developmental Disorders, 31*(3), 265–77.

Hoekstra, R.A., Bartels, M., Cath, D.C., Boomsma, D.I., et al. (2008). Factor structure, reliability and criterion validity of the Autism-Spectrum Quotient (AQ): a study in Dutch population and patient groups. *Journal of Autism and Developmental Disorders, 38*(8), *1555–66.*

Hollander, E., Anagnostou, E., Winterrowd, E., et al. (2005). Striatal volume on magnetic resonance imaging and repetitive behaviors in autism. *Biological Psychiatry, 58*(3), 226–32.

Jiao, Y., Chen, R., Ke, X., et al. (2010). Predictive models of autism spectrum disorder based on brain regional cortical thickness. *Neuroimage, 50*(2), 589–99.

Kringelbach, M.L., Rolls, E.T. (2004). The functional neuroanatomy of the human orbitofrontal cortex: evidence from neuroimaging and neuropsychology. *Progress in Neurobiology, 72*(5), 341–72.

Kurita, H., Koyama, T., Osada, H., et al. (2005). Autism-Spectrum Quotient-Japanese version and its short forms for screening normally intelligent persons with pervasive developmental disorders. *Psychiatry and Clinical Neuroscience, 59*(4), 490–6.

Lauvin, M.A., Martineau, J., Destrieux, C., et al. (2012). Functional morphological imaging of autism spectrum disorders: current position and theories proposed. *Diagnostic and Interventional Imaging, 93*(3), 139–47.

Lewis, M., Kim, S.J. (2009). The pathophysiology of restricted repetitive behavior. *Journal of Neurodevelopmental Disorders, 1*(2), 114–32.

Lohmann, G., von Cramon, D.Y., Steinmetz, H., et al. (1999). Sulcal variability of twins. *Cerebral Cortex, 9*(7), 754–63.

Luders, E., Kurth, F., Mayer, E.A., et al. (2012). The unique brain anatomy of meditation practitioners: alterations in cortical gyrification. *Frontiers in Human Neuroscience, 6*, 34.

Maia, T.V., Cooney, R.E., Peterson, B.S., et al. (2008). The neural bases of obsessive-compulsive disorder in children and adults. *Development and Psychopathology, 20*(4), 1251–83.

Mandy, W.P., Charman, T., Skuse, D.H., et al. (2012). Testing the construct validity of proposed criteria for DSM-5 autism spectrum disorder. *Journal of the American Academy of Child and Adolescent Psychiatry, 51*(1), 41–50.

Marco, E.J., Hinkley, L.B., Hill, S.S., Nagarajan, S.S. (2011). Sensory processing in autism: a review of neurophysiologic findings. *Pediatric Research, 69*(5 Pt 2), 48R–54R.

Matsuoka, K., Kim, Y. (2006). *Japanese Adult Reading Test (JART).* Tokyo: Shinkou-igaku Publication.

Muhle, R., Trentacoste, S.V., Rapin, I. (2004). The genetics of autism. *Pediatrics, 113*(5), e472–86.

Nakamura, M., Nestor, P.G., McCarley, R.W., et al. (2007). Altered orbitofrontal sulcogyral pattern in schizophrenia. *Brain, 130*(Pt 3), 693–707.

Nakamura, M., Nestor, P.G., Levitt, J.J., et al. (2008). Orbitofrontal volume deficit in schizophrenia and thought disorder. *Brain, 131*(Pt 1), 180–95.

Nelson, H.E., Willison, J.R. (1991). *National Adult Reading Test (NART)* 2nd edn. Windsor, UK: NFER-Nelson.

Oldfield, R.C. (1971). The assessment and analysis of handedness: the Edinburgh inventory. *Neuropsychologia, 9*(1), 97–113.

Ongur, D., Ferry, A.T., Price, J.L. (2003). Architectonic subdivision of the human orbital and medial prefrontal cortex. *Journal of Comparative Neurology, 460*(3), 425–49.

Otsubo, T., Kamijima, K. (2000). *The Japanese Version of The Mini-International NEuropsychiatric Interview (M.I.N.I): The Development and Validation of a Structured Diagnostic Psychiatric Interview for DSM-IV and ICD-10.* Tokyo: Seiwa Bookstore.

Parnas, J. (2011). A disappearing heritage: the clinical core of schizophrenia. *Schizophrenia Bulletin, 37*(6), 1121–30.

Philip, R.C., Dauvermann, M.R., Whalley, H.C., et al. (2012). A systematic review and meta-analysis of the fMRI investigation of autism spectrum disorders. *Neuroscience and Biobehavioral Reviews, 36*(2), 901–42.

Rakic, P. (1988). Specification of cerebral cortical areas. *Science, 241*(4862), 170–6.

Rapoport, J., Chavez, A., Greenstein, D., Addington, A., Gogtay, N. (2009). Autism spectrum disorders and childhood-onset schizophrenia: clinical and biological contributions to a relation revisited. *Journal of the American Academy of Child and Adolescent Psychiatry, 48*(1), 10–8.

Rojas, D.C., Peterson, E., Winterrowd, E., et al. (2006). Regional gray matter volumetric changes in autism associated with social and repetitive behavior symptoms. *BMC Psychiatry, 6*, 56.

Roppongi, T., Nakamura, M., Asami, T., et al. (2010). Posterior orbitofrontal sulcogyral pattern associated with orbitofrontal cortex volume reduction and anxiety trait in panic disorder. *Psychiatry and Clinical Neurosciences, 64*(3), 318–26.

Rotge, J.Y., Guehl, D., Dilharreguy, B., et al. (2009). Meta-analysis of brain volume changes in obsessive-compulsive disorder. *Biological Psychiatry, 65*(1), 75–83.

Schoenbaum, G., Roesch, M. (2005). Orbitofrontal cortex, associative learning, and expectancies. *Neuron, 47*(5), 633–6.

Sears, L.L., Vest, C., Mohamed, S., et al. (1999). An MRI study of the basal ganglia in autism. *Progress in Neuropsychopharmacology and Biological Psychiatry, 23*(4), 613–24.

Sebat, J., Lakshmi, B., Malhotra, D., et al. (2007). Strong association of de novo copy number mutations with autism. *Science, 316*(5823), 445–9.

Solomon, M., Olsen, E., Niendam, T., et al. (2011). From lumping to splitting and back again: atypical social and language development in individuals with clinical-high-risk for psychosis, first episode schizophrenia, and autism spectrum disorders. *Schizophrenia Research, 131*(1–3), 146–51.

Stenger, V.A. (2006). Technical considerations for BOLD fMRI of the orbitofrontal cortex. In: Zald David, H., Rauch Scott, L., editors. *The Orbitofrontal Cortex.* Oxford: Oxford University Press, pp. 423–46.

Sugranyes, G., Kyriakopoulos, M., Corrigall, R., Taylor, E., Frangou, S. (2011). Autism spectrum disorders and schizophrenia: meta-analysis of the neural correlates of social cognition. *PLoS ONE, 6*(10), e25322.

Takayanagi, Y., Takahashi, T., Orikabe, L., et al. (2010). Volume reduction and altered sulco-gyral pattern of the orbitofrontal cortex in first-episode schizophrenia. *Schizophrenia Research, 121*(1–3), 55–65.

Toro, R., Burnod, Y. (2005). A morphogenetic model for the development of cortical convolutions. *Cerebral Cortex, 15*(12), 1900–13.

Turner, M. (1999). Annotation: repetitive behaviour in autism: a review of psychological research. *Journal of Child Psychology and Psychiatry, 40*(6), 839–49.

Uehara-Aoyama, K., Nakamura, M., Asami, T., et al. (2011). Sexually dimorphic distribution of orbitofrontal sulcogyral pattern in schizophrenia. *Psychiatry and Clinical Neurosciences, 65*(5), 483–9.

Urfer-Parnas, A., Mortensen, E.L., Parnas, J., et al. (2010). Core of schizophrenia: estrangement, dementia or neurocognitive disorder? *Psychopathology, 43*(5), 300–11.

Van Essen, D.C. (1997). A tension-based theory of morphogenesis and compact wiring in the central nervous system. *Nature, 385*(6614), 313–8.

Via, E., Radua, J., Happe, F., Mataix-Cols, D. (2011). Meta-analysis of gray matter abnormalities in autism spectrum disorder: should Asperger disorder be subsumed under a broader umbrella of autistic spectrum disorder? *Archives of General Psychiatry, 68*(4), 409–18.

Wakabayashi, A., Baron-Cohen, S., Wheelwright, S., Tojo, Y. (2006). The Autism-Spectrum Quotient (AQ) in Japan: a cross-cultural comparison. *Journal of Autism and Developmental Disorders, 36*(2), 263–70.

Medical Physics
The International Journal of Medical Physics Research and Practice

Intensity inhomogeneity correction for magnetic resonance imaging of human brain at 7T

Ikuko Uwano, Kohsuke Kudo, Fumio Yamashita, Jonathan Goodwin, Satomi Higuchi, Kenji Ito, Taisuke Harada, Akira Ogawa, and Makoto Sasaki

Citation: Medical Physics **41**, 022302 (2014); doi: 10.1118/1.4860954
View online: http://dx.doi.org/10.1118/1.4860954
View Table of Contents: http://scitation.aip.org/content/aapm/journal/medphys/41/2?ver=pdfcov
Published by the American Association of Physicists in Medicine

Intensity inhomogeneity correction for magnetic resonance imaging of human brain at 7T

Ikuko Uwano
Division of Ultrahigh Field MRI, Institute for Biomedical Sciences, Iwate Medical University, Yahaba, Iwate 028-3694, Japan

Kohsuke Kudo[a)]
Division of Ultrahigh Field MRI, Institute for Biomedical Sciences, Iwate Medical University, Yahaba, Iwate 028-3694, Japan and Department of Diagnostic and Interventional Radiology, Hokkaido University Hospital, Sapporo, Hokkaido 060-8648, Japan

Fumio Yamashita
Division of Ultrahigh Field MRI, Institute for Biomedical Sciences, Iwate Medical University, Yahaba, Iwate 028-3694, Japan

Jonathan Goodwin
Division of Ultrahigh Field MRI, Institute for Biomedical Sciences, Iwate Medical University, Yahaba, Iwate 028-3694, Japan and Department of Diagnostic and Interventional Radiology, Hokkaido University Hospital, Sapporo, Hokkaido 060-8648, Japan

Satomi Higuchi and Kenji Ito
Division of Ultrahigh Field MRI, Institute for Biomedical Sciences, Iwate Medical University, Yahaba, Iwate 028-3694, Japan

Taisuke Harada
Division of Ultrahigh Field MRI, Institute for Biomedical Sciences, Iwate Medical University, Yahaba, Iwate 028-3694, Japan and Department of Diagnostic and Interventional Radiology, Hokkaido University Hospital, Sapporo, Hokkaido 060-8648, Japan

Akira Ogawa
Department of Neurosurgery, Iwate Medical University, Morioka, Iwate 020-8505, Japan

Makoto Sasaki
Division of Ultrahigh Field MRI, Institute for Biomedical Sciences, Iwate Medical University, Yahaba, Iwate 028-3694, Japan

(Received 7 August 2013; revised 21 November 2013; accepted for publication 17 December 2013; published 14 January 2014)

Purpose: To evaluate the performance and efficacy for intensity inhomogeneity correction of various sequences of the human brain in 7T MRI using the extended version of the unified segmentation algorithm.
Materials: Ten healthy volunteers were scanned with four different sequences (2D spin echo [SE], 3D fast SE, 2D fast spoiled gradient echo, and 3D time-of-flight) by using a 7T MRI system. Intensity inhomogeneity correction was performed using the "New Segment" module in SPM8 with four different values (120, 90, 60, and 30 mm) of full width at half maximum (FWHM) in Gaussian smoothness. The uniformity in signals in the entire white matter was evaluated using the coefficient of variation (CV); mean signal intensities between the subcortical and deep white matter were compared, and contrast between subcortical white matter and gray matter was measured. The length of the lenticulostriate (LSA) was measured on maximum intensity projection (MIP) images in the original and corrected images.
Results: In all sequences, the CV decreased as the FWHM value decreased. The differences of mean signal intensities between subcortical and deep white matter also decreased with smaller FWHM values. The contrast between white and gray matter was maintained at all FWHM values. LSA length was significantly greater in corrected MIP than in the original MIP images.
Conclusions: Intensity inhomogeneity in 7T MRI can be successfully corrected using SPM8 for various scan sequences. © *2014 American Association of Physicists in Medicine.* [http://dx.doi.org/10.1118/1.4860954]

Key words: 7T, MRI, intensity inhomogeneity correction

1. INTRODUCTION

Recent advancement of ultra-high field MR systems has enabled the use of 7T MRI for clinical research, and these systems are steadily increasing in number. Ultra-high field MRI offers several advantages over conventional clinical MRI (3.0T or below), such as higher signal-to-noise ratio, higher spatial resolution, better image contrast, prolonged T1 relaxation time, and increased susceptibility effects.[1,2] However, intensity variation or inhomogeneity are remarkable at 7T because of main magnetic field (B_0) and radio frequency (RF) field (B_1) inhomogeneity,[1,3,4] susceptibility effects,[1,4–6] and use of a multichannel surface coil.[1,4,7] Among these factors, B_1 inhomogeneity is of particular importance in 7T brain imaging,[8] in which RF wavelength becomes similar to the diameter of the human head.[9,10] These intensity inhomogeneities may cause under-representation of lesions and must be minimized in clinical imaging.[11]

Bias correction of intensity inhomogeneity is categorized into prospective and retrospective approaches (see Refs. 12 and 13 for details). Prospective approaches aim to acquire more uniform signal distribution by improving the imaging device, such as the development of special sequence designs or parallel transmission with B_1 shimming[14,15] or a modified RF pulse.[16,17] These prospective developments are more difficult to apply than retrospective methods, because intensity uniformity varies among sequence types as well as among tissues and subjects. In contrast, retrospective approaches are postprocessing techniques applied to the acquired images. These approaches are independent of special hardware or sequence designs and are used for correcting intensity nonuniformity in the acquired images. Previous reports have reviewed the techniques proposed to correct intensity inhomogeneity,[12,13] e.g., nonparametric nonuniform intensity normalization (N3),[18] BrainSuite,[19,20] and statistical parametric mapping (SPM) [SPM99 (Ref. 21) of old version, SPM2,[22] SPM5 (Ref. 23) and SPM8 (Refs. 23 and 24) of newer version]. A quantitative comparison of these methods[25–29] has also been performed for human brain imaging at 3.0T or below. For 7T, however, the performance of retrospective correction approaches has not been investigated in human brain imaging, although studies have been performed that validated the approaches by using phantom data[30] or that introduced the results when the approaches were applied to human brain images.[31]

The purpose of this study was to evaluate the performance and efficacy of a postprocessing technique using the extended version of the unified segmentation algorithm available with SPM8 (http://www.fil.ion.ucl.ac.uk/spm/) (Refs. 23 and 24) for intensity inhomogeneity correction of various sequences of the human brain in 7T MRI.

2. METHODS

2.A. Subjects

Ten healthy volunteers [six men (mean age, 29.5 years; age range, 24–39 years) and four women (mean age, 31.8 years; age range, 28–34 years)] were included in the study, which was conducted between June 13 and July 12, 2012. These volunteers were confirmed to have no past history or symptom of brain disorders. All experiments were carried out after obtaining the approval of the institutional review board and written informed consent from all subjects.

2.B. 7T MRI

We used a 7T MRI scanner (Discovery MR950; GE Healthcare, Milwaukee, WI) with quadrature transmission and 32-channel receive head coils. The examination consisted of four different sequences: 2D spin echo (2D-SE), 3D fast SE (3D-FSE), 2D fast spoiled gradient echo (2D-FSPGR), and 3D time-of-flight (3D-TOF) (Table I).

2.C. Intensity inhomogeneity correction using SPM8

Intensity inhomogeneity correction was performed using the "New Segment" module in SPM8, which is the extended version of the unified segmentation algorithm implemented in SPM8 (Refs. 23 and 24) adopting an extended set of

TABLE I. MRI parameters used in this study.

	2D-SE	3D-FSE	2D-FSPGR	3D-TOF
Repetition time (ms)	3000	3000	800	14
Echo time (ms)	60	60	15	2.9
Excitation flip angle (deg)	90	90	20	12
Refocusing flip angle (deg)	140	Variable	n/a	n/a
Receive bandwidth (kHz)	62.5	83.33	62.5	35.7
Number of excitations	0.5	1	1	1
Scan time	5 min 48 s	7 min 12 s	2 min 40 s	8 min 7 s
Field of view (mm)	256	256	256	256
Slice thickness (mm)	4	1	4	1
Acquisition matrix	512 × 256	512 × 256	512 × 256	512 × 256
Reconstruction matrix	512 × 512	512 × 512	512 × 512	512 × 512
Reconstruction voxel (mm)	0.5 × 0.5 × 4	0.5 × 0.5 × 0.5	0.5 × 0.5 × 4	0.5 × 0.5 × 0.5

Note: 2D-SE, 2D spin echo; 3D-FSE, 3D fast spin echo; 2D-FSPGR, 2D fast spoiled gradient echo; 3D-TOF, 3D time-of-flight.

tissue probability maps and improved registration model. The algorithm implements segmentation, bias correction, and spatial normalization in one step, and the underlying generative model includes a correction for intensity nonuniformity and is estimated for a maximum *a posteriori* solution. For the parameter of full width at half maximum (FWHM) in Gaussian smoothness, the operator can select values from 30 to 150 mm (with an interval of 10 mm) on the graphical user interface, although any other value can be set by modifying the script file. If the acquired MR image has conspicuous inhomogeneous intensities, the operator can select a smaller FWHM value (default value in SPM8 is 60 mm). We used four different FWHM values (120, 90, 60, and 30 mm) and default parameters including bias regularization of 0.0001, warping regularization of 4, and sampling distance of 3; in addition, the number of Gaussians used to represent the intensity distribution for each tissue class was 2 for grey matter, 2 for white matter, 2 for CSF, 3 for bone, 4 for other soft tissues, and 2 for air (background).

2.D. Data analysis

Eight sections, the middle of which was at the level of the centrum semiovale, were chosen for ROI measurements (every 2 and 16 sections for 2D and 3D sequences, respectively, as the sections were thicker in 2D). Using ITK-SNAP (www.itksnap.org),[32] one of the authors (I.U.) manually drew eight spherical ROIs with a diameter of 2.5 mm on each section, in the subcortical and deep white-matter areas, respectively (total 16 ROIs $\times$ 8 sections). ROIs with the same size were also placed in the gray-matter areas near the ROIs of subcortical white matter (total 8 ROIs $\times$ 8 sections). All ROIs were carefully placed in the white matter having uniform intensity while avoiding areas with intensity variation such as the optic radiation, perivascular space, and small arteries. Because 3D-FSE images were taken as sagittal sections, the ROI measurements for 3D-FSE images were performed on the reformatted axial sections (slice thickness of 0.5 mm).

For the evaluation of signal uniformity in the entire white matter, we calculated the coefficient of variation (CV),[33] defined as the ratio of the standard deviation and the mean signal intensity for all ROIs (both subcortical and deep white matter). A smaller CV represented more uniform signals in the entire white matter. The Steel–Dwass test was used for nonparametric multiple comparisons between CV values of the original and corrected images using four different FWHM values ($p < 0.01$). For the evaluation of the signal variation between the subcortical and deep white-matter images, mean signal intensities of ROIs were compared between the subcortical and deep white-matter images with the Wilcoxon matched-pairs signed-ranks test ($p < 0.01$). If the difference of mean signal intensities between both white matters was smaller values, it represented more improvement of signal drop in the center of the brain. Moreover, for evaluation of the impact of inhomogeneity correction on the contrast between different tissues, we calculated the contrast ratio between the subcortical white matter and gray matter. The Wilcoxon matched-pairs signed-ranks test with Bonferroni adjustment was used for multiple comparisons between contrast ratios of the original and corrected images using four different FWHM values ($p < 0.01$ after Bonferroni adjustment).

The efficacy of intensity correction on the maximum intensity projection (MIP) image in MR angiography (MRA) was also evaluated. Coronal MIP images (thickness of 70 mm), including anterior and middle cerebral arteries, lenticulostriate arteries (LSA), and basal ganglia, were reconstructed from 3D-TOF original and corrected images with the best FWHM value decided by two evaluations (CVs and signal intensities in the subcortical and deep white matter). Basilar and posterior cerebral arteries were excluded because the posterior cerebral artery mimics the LSA on coronal MIP images. MIP reconstructions were performed by one of the authors (I.U.) using a commercially available workstation (Advantage Workstation 4.5; GE Medical Systems, Milwaukee, WI).

In evaluations of MIP images, we compared the length of the LSA in 3D-TOF original and corrected MIP images, because the LSA located in the center of the brain is most severely affected by the signal drop in the center of the 3D-TOF image in particular. Then, two radiologists (K.K. and T.H. with 17 and 4 years of experience, respectively) independently measured the length of the longest LSA (right and left, respectively) on MIP images by using commercially available software (VOX-BASE II; J-MAC SYSTEM, Sapporo, Japan). The interobserver variability of LSA measurements was assessed using the intraclass correlation coefficient (ICC). The Wilcoxon matched-pairs signed-ranks test was used to evaluate differences of mean length of the LSA between the original MIP and SPM8-corrected MIP images.

3. RESULTS

The signals in the central part of the brain in the original axial images were weaker than those in the peripheral part (Fig. 1), which was most noticeable in 3D-TOF images. In addition, signals were stronger in the lower left part than in the other parts in SE sequences (2D-SE and 3D-FSE images). The caudal part in sagittal 3D-FSE images also had weaker signals. All of these intensity inhomogeneities were successfully corrected using SPM8 with decreasing FWHM values.

The CV constantly decreased as the FWHM value decreased for all imaging sequences (Fig. 2), indicating that signal intensities in the white matter became homogeneous. In 3D-TOF images, the differences were statistically significant for all pairs of FWHM values ($p < 0.01$ for all pairs). In the 2D-SE, 2D-FSPGR, and 3D-FSE images, most of the pairs showed statistically significant differences, with a few exceptions.

In all sequences, mean signal intensities had significantly higher values in the subcortical white matter than in the deep white matter in the original images (Fig. 3). After correction of intensity inhomogeneity, the difference of signal intensities between subcortical and deep white matter decreased; however, there were still significant differences between FWHM values of 120 and 90 mm in all sequences. With an FWHM value of 60 mm, the differences in the white-matter signals

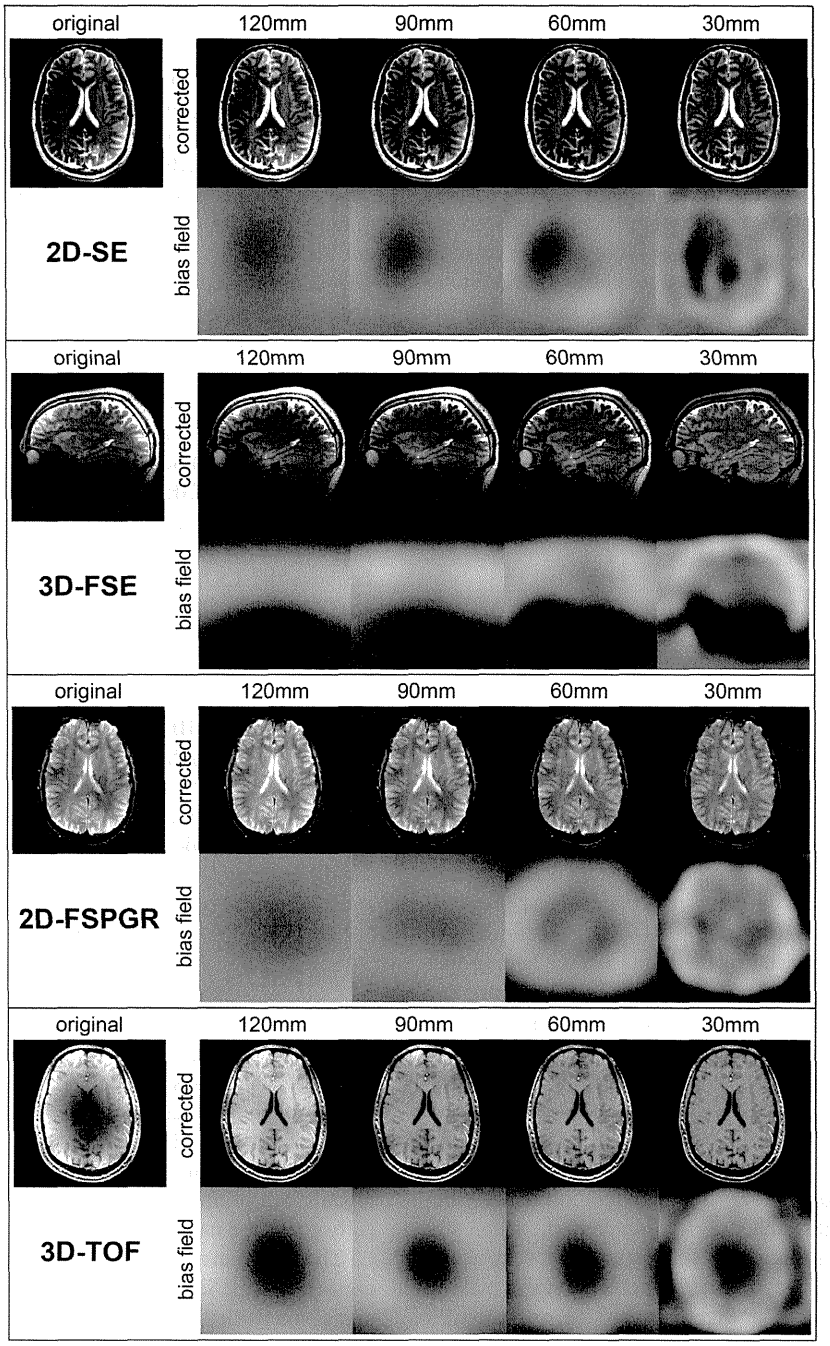

FIG. 1. Original and SPM8-corrected images. In the original images, the signals in the central parts of the axial images (2D-SE, 2D-FSPGR, and 3D-TOF) and caudal parts of the sagittal 3D-FSE image are weaker than those in the other parts. These intensity inhomogeneities are reduced as the FWHM values decrease in all sequences. The estimated bias field, which represents the distribution map of intensity inhomogeneity that was calculated by SPM8 with each FWHM value, is shown at the bottom. Decreased FWHM value tends to strengthen the signal variations of estimated bias field images.

became nonsignificant in all sequences, while the differences became significant again with an FWHM value of 30 mm for the two gradient echo (GRE) sequences (2D-FSPGR and 3D-TOF).

In the contrast ratio between white and gray matter, there were no statistically significant differences in all sequences (Table II), indicating that inhomogeneity correction in SPM8 maintained the contrast between white and gray matter ($p > 0.05$ for all pairs).

In MIP images, the corrected MIP image was created from the corrected 3D-TOF image with an FWHM value of 30 mm, which was decided by two evaluations of CVs (Fig. 2) and signal intensities in the subcortical and deep white matter (Fig. 3). The LSAs and distal arteries were better seen in the

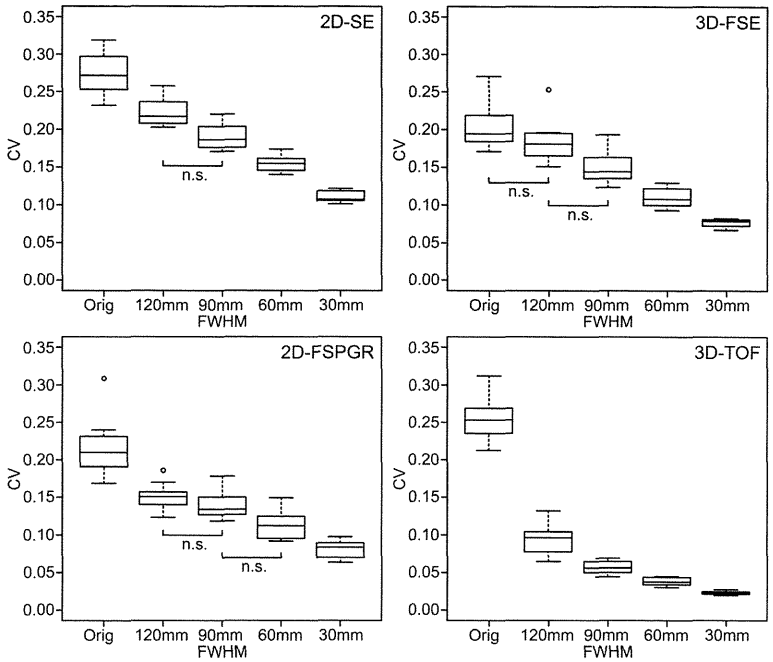

FIG. 2. Coefficient of variation (CV) for the original and SPM8-corrected images. In all sequences, the CV decreases as the FWHM value decreases, indicating that the white-matter signals become homogeneous. In the 3D-TOF, the differences are statistically significant for all pairs of FWHM values (Steel–Dwass test, $p < 0.01$ for all pairs). In the 2D-SE, 2D-FSPGR, and 3D-FSE, most of the pairs show statistically significant differences, although there are a few exceptions. n.s. indicates no significant difference.

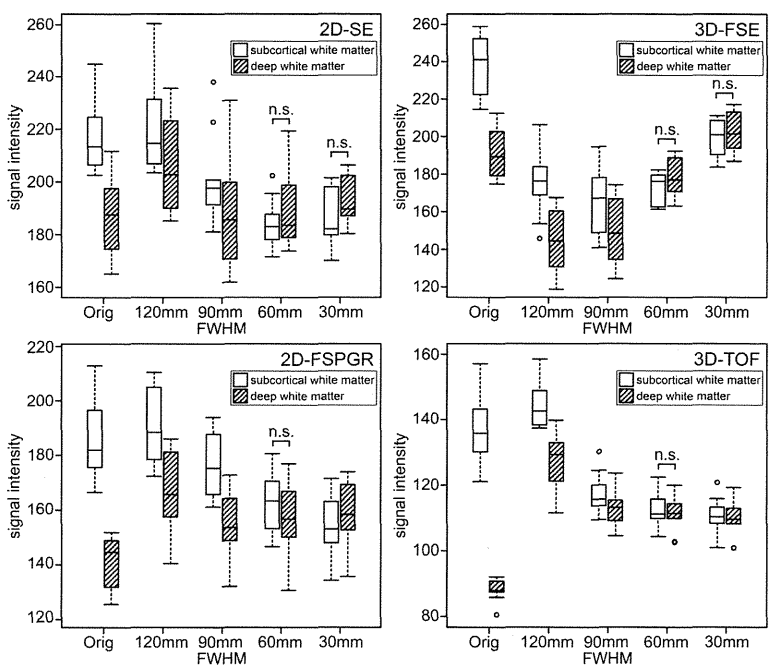

FIG. 3. Mean signal intensities of subcortical and deep white matter. In the original images of all sequences, mean signal intensities in the subcortical white matter have significantly higher values than in the deep white matter. After correction of intensity inhomogeneity, the difference of signal intensities between subcortical and deep white matter decreases; however, there are still significant differences between FWHM values of 120 and 90 mm in all sequences (Wilcoxon matched-pairs signed-ranks test, $p < 0.01$). With an FWHM value of 60 mm in all sequences, the differences of signal intensities between subcortical and deep white matter are nonsignificant; however, the differences are significant again with an FWHM value of 30 mm for the two GRE sequences (2D-FSPGR and 3D-TOF). n.s. indicates no significant difference.

TABLE II. Contrast ratio between subcortical white matter and gray matter (subcortical white matter ROI/gray matter ROI).

	FWHM				
	Original	120 mm	90 mm	60 mm	30 mm
2D-SE	0.80 ± 0.07	0.80 ± 0.06	0.80 ± 0.06	0.80 ± 0.06	0.81 ± 0.05
3D-FSE	0.79 ± 0.03	0.79 ± 0.03	0.79 ± 0.03	0.80 ± 0.03	0.81 ± 0.03
2D-FSPGR	0.78 ± 0.03	0.79 ± 0.03	0.79 ± 0.03	0.80 ± 0.03	0.80 ± 0.03
3D-TOF	1.07 ± 0.02	1.09 ± 0.02	1.08 ± 0.02	1.08 ± 0.02	1.08 ± 0.02

Note: 2D-SE, 2D spin echo; 3D-FSE, 3D fast spin echo; 2D-FSPGR, 2D fast spoiled gradient echo; 3D-TOF, 3D time-of-flight.

corrected MIP image compared with the original MIP image, in which the central part of the brain was darker than the peripheral part (Fig. 4). The measured LSA length was significantly greater in the corrected than original MIP images (Fig. 5). The ICC of interobserver variability for LSA measurements was 0.86.

4. DISCUSSION

In this study, we tested the performance of intensity inhomogeneity correction using SPM8 for various scan sequences of the human brain at 7T and evaluated the efficacy of the correction with various FWHM values in Gaussian smoothness. We found that inhomogeneity correction in the 7T MR images was more effective with smaller FWHM values. The RF wavelength decreases with increasing field strength, and when it is shorter than the dimensions of the human head, constructive interferences of standing waves occur.[9,10] This produces a very inhomogeneous RF distribution and, consequently, inhomogeneous signal variation is seen across the image. The standing wave effects at 7T lead to more pronounced B_1 inhomogeneities compared with 3T and below. Although this intensity inhomogeneity is low frequency compared with anatomical brain structures, the inhomogeneity with greater field strength may modulate to a higher frequency or increase low-frequency bandwidth; therefore, inhomogeneity correction using SPM8 may require lower FWHM (smoothness constants of the bias field) values to obtain uniform image intensity at 7T. Any FWHM parameter in SPM8 can be chosen by modifying the script file used to run the New Segment module; however, the smallest FWHM value on the graphical user interface is 30 mm, so we used FWHM values of 30–120 mm. In our study, the best FWHM value was considered 30 mm. Weiskopf *et al.*,[24] who introduced New Segment in SPM8, reported that the optimal FWHM value at 3T was 60 mm for R1 (longitudinal relaxation rate) brain maps using dual angle FLASH imaging (testing range, 30–150 mm). In addition, our study revealed that New Segment in SPM8 for 7T can also correct intensity inhomogeneities better with smaller FWHM values than the default value of 60 mm (which was determined for 3T or below on conventional clinical MRI). Therefore, the optimal FWHM value tends to decrease with increasing magnetic field strength. In the two GRE sequences, however, the difference of signal intensity between the subcortical and deep white matter was statistically significant with an FWHM value of 30 mm, although there were no significant differences at 60 mm. This was probably due to overcorrection of intensity inhomogeneity, and the

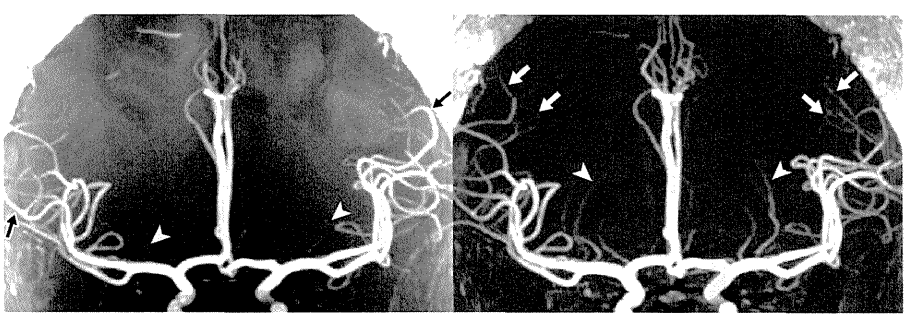

FIG. 4. Original and corrected MIP images in 3D-TOF. Maximum intensity projection (MIP) images of 70-mm slabs, showing the horizontal portion of the middle cerebral artery, have been created from the original 3D-TOF image (left) and SPM8-corrected image with an FWHM value of 30 mm (right). As the mean signal intensities were changed by the correction of the inhomogeneity at each FWHM value (see Fig. 3), both MIP images were normalized with an optimal window level and width. ROI measurements of the M1 segment of the middle cerebral artery were completed, and the maximum value of the ROI was used for determination of the window level and width (maximum value × 0.4 for window level, and maximum value × 0.5 for window width). The lenticulostriate arteries (arrowheads) are seen more clearly in the corrected MIP image than in the original MIP image. Although some distal branches of the middle cerebral artery (MCA) are thicker and/or brighter in the original image (black arrows) than in the corrected MIP image, most peripheral MCA branches are seen more clearly in the corrected MIP image (white arrows). Note that brain parenchyma is visible in the original MIP image and that the central part of the brain is darker than the peripheral part.

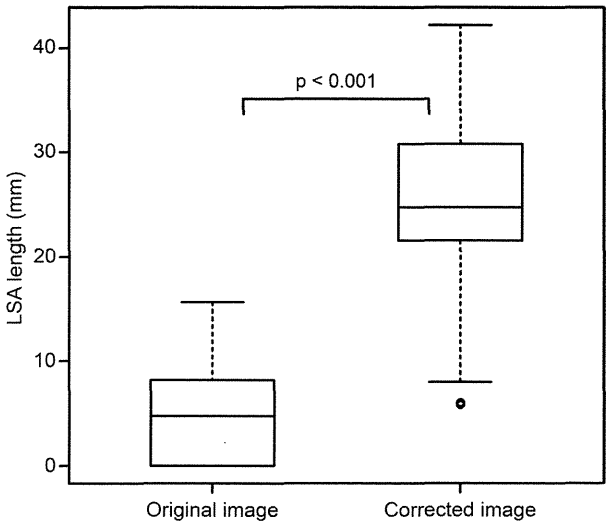

FIG. 5. Comparison of LSA length in the original and corrected MIP images. LSA length measured in the corrected MIP image is significantly greater than that in the original MIP image (Wilcoxon matched-pairs signed-ranks test, $p < 0.001$).

best FWHM value for GRE sequences might be between 60 and 30 mm. However, further evaluation is needed to clarify this issue (see limitations below).

There are concerns that inhomogeneity correction with retrospective methods may have undesirable effects such as reduction of the contrast between different tissue types. We found that the contrast between white and gray matter was maintained after inhomogeneity correction at four FWHM values in SPM8. Tissue probability maps in the unified segmentation implemented in SPM may have the favorable effect of maintaining contrasts between different tissue types. However, the contrast between different tissues may be reduced at FWHM values of less than 30 mm because of overcorrection of intensity inhomogeneity (see limitations below).

Without intensity correction, signal intensities of clinical images at 7T are inhomogeneous and may negatively affect clinical diagnosis on visual inspection. For example, it has been discussed that subpial lesions in multiple sclerosis may not be detected because of intensity nonuniformity.[11] Therefore, intensity inhomogeneities should be reduced or minimized by applying intensity inhomogeneity correction. Inhomogeneity correction has also been reported to improve accuracy and reliability of various computational analysis techniques such as anatomical tissue classification and cortical segmentation and registration.[29,34] MR angiography at 7T has enabled imaging of microvasculature including smaller peripheral vessels;[35,36] however, as shown in the results of our experiments (Figs. 4 and 5), small perforating arteries in the middle of the brain, such as the LSA, could not be well visualized on MIP images without intensity correction because the center of the brain has low signal intensity in the original image at 7T. Reduction of intensity inhomogeneity in MR angiography provided clear anatomic delineation of the microvasculature and is, therefore, likely to play an important role in clinical assessment of microvasculature imaging.

There are 2 types of correction methods for intensity inhomogeneities, prospective and retrospective procedures. The retrospective, postprocessing methods, such as SPM8 used in this study, are able to simply correct intensity inhomogeneity without any special hardware or sequence designs; however, the areas of severe signal loss cannot be recovered or corrected because the corrupted source signal cannot be regenerated. On the other hand, the prospective methods can minimize signal error during the MR image-acquisition process by applying (1) RF shimming, where the channels of the transmitting coil are driven with tunable global RF phase and amplitude to optimize homogeneity of the resulting B_1 field,[14,15] (2) parallel transmission techniques, which use multiple excitation coils driven by independent RF pulses,[37] or (3) special imaging sequences.[38] Although these methods are still under development in the ultra-high field over 7T, it is expected that these procedures or hardware will be incorporated into commercial MRI in the near future.

In the original images, signal drop in the center of the brain was more remarkable in GRE sequences (2D-FSPGR and 3D-TOF) than in SE and FSE images. This may be explained by the GRE sequence having a smaller flip angle, single excitation RF pulse (i.e., no refocusing RF pulse), and shorter repetition time (TR).[39] Hence, GRE sequence images are less affected by B_1 inhomogeneity and more strongly influenced by inhomogeneous coil sensitivity. As a result, the signal drop is more remarkable in the area distant to the surface coils. In contrast, the SE sequence has 2 RF pulses with a larger flip angle of excitation together with refocusing, and a longer TR. Therefore, SE is more susceptible to B_1 inhomogeneity than inhomogeneous coil sensitivity.[3,10,40] Both types of inhomogeneities have similar low-frequency components in MR signal intensity; therefore, SPM8 used as a postprocessing method in our study successfully corrected intensity inhomogeneities of B_1 fields and coil sensitivity at 7T.

This study has several limitations. First, CV was used for the evaluation of correction performance of intensity inhomogeneity correction. CV has been commonly used to evaluate correction performance in conventional MRI at 3.0T or below, and it assumes that the signals in the entire white matter are uniform. However, white matter signals are not necessarily uniform because white-matter structures including different fibers and microvasculature have intensity variation. Therefore, smaller CV values may not necessarily reflect the best correction results. However, because ROIs in our experiments were located avoiding white-matter structures with intensity variation, such as fibers and microvasculature, CV was considered appropriate for correction performance in our study. Second, the best FWHM value for inhomogeneous signal correction in 7T images was considered 30 mm; however, we did not test FWHM values below 30 mm because this is the smallest value that can be selected on the graphical user interface of New Segment in SPM8. However, FWHM values less than 30 mm may cause erroneous correction as a result of reduced contrast between white matter and gray matter due to overfitting to the model.[23,33] Moreover, further study might be needed to evaluate the correction performance in FWHM values between 60 and 30 mm, because the best FWHM value

for GRE sequences might be between 60 and 30 mm. Third, although the best FWHM value in our tests was 30 mm, further studies are needed, such as visual inspection by expert radiologists, to confirm that smaller FWHM values result in better clinical performance in lesion detection and diagnosis. Fourth, our study modified only FWHM value among all tunable parameters in the New Segment module. Further study is needed to evaluate correction performances at 7T with various combinations of parameters. Fifth, although our study used SPM8 as a technique for correcting nonuniformity in 7T MR images, there are several other techniques and software such as N3,[18] BrainSuite,[19,20] and BrainVoyager (http://www.brainvoyager.com; Brain Innovation, Maastricht, Netherlands). Further study is needed to evaluate correction performances at 7T of these approaches. Sixth, we examined images from healthy volunteers only. Further studies are needed to evaluate performance in signal correction by SPM8 in patient groups with various brain disorders, in which SPM8 may produce incorrect results such as less contrast between the lesion and surrounding normal tissue, or overcorrection.

In conclusion, the intensity inhomogeneities caused by both inhomogeneous B_1 field and coil sensitivity in 7T MRI were successfully corrected using SPM8 for various clinical sequences. In Gaussian smoothness, smaller FWHM values yielded better results in correction of intensity inhomogeneity, and the best FWHM value was considered 30 mm for the sequences evaluated in this study.

ACKNOWLEDGMENTS

This work was supported by a Grant-in-Aid for the Strategic Medical Science Research Center from the Ministry of Education, Culture, Sports, Science and Technology of Japan and the Japan Society for the Promotion of Science (JSPS) through the "Funding Program for the Next Generation World-Leading Researchers (NEXT Program)" initiated by the Council for Science and Technology Policy (CSTP) and JSPS KAKENHI Grant No. 13281909 (Grant-in-Aid for Young Scientists (B) to UI). The authors declare that they have no conflict of interest.

[a]Author to whom correspondence should be addressed. Electronic mail: kkudo@huhp.hokudai.ac.jp; Telephone: +81-19-651-5111; Fax: +81-19-908-8021.

[1]E. Moser, F. Stahlberg, M. E. Ladd, and S. Trattnig, "7-T MR–from research to clinical applications?," NMR Biomed. **25**(5), 695–716 (2012).

[2]K. Ugurbil, G. Adriany, P. Andersen, W. Chen, M. Garwood, R. Gruetter, P. G. Henry, S. G. Kim, H. Lieu, I. Tkac, T. Vaughan, P. F. Van De Moortele, E. Yacoub, and X. H. Zhu, "Ultrahigh field magnetic resonance imaging and spectroscopy," Magn. Reson. Imaging **21**(10), 1263–1281 (2003).

[3]T. K. Truong, D. W. Chakeres, D. Q. Beversdorf, D. W. Scharre, and P. Schmalbrock, "Effects of static and radiofrequency magnetic field inhomogeneity in ultra-high field magnetic resonance imaging," Magn. Reson. Imaging **24**(2), 103–112 (2006).

[4]J. N. Morelli, V. M. Runge, F. Ai, U. Attenberger, L. Vu, S. H. Schmeets, W. R. Nitz, and J. E. Kirsch, "An image-based approach to understanding the physics of MR artifacts," Radiographics **31**(3), 849–866 (2011).

[5]J. D. Port and M. G. Pomper, "Quantification and minimization of magnetic susceptibility artifacts on GRE images," J. Comput. Assist. Tomogr. **24**(6), 958–964 (2000).

[6]V. A. Stenger, F. E. Boada, and D. C. Noll, "Three-dimensional tailored RF pulses for the reduction of susceptibility artifacts in T(*)(2)-weighted functional MRI," Magn. Reson. Med. **44**(4), 525–531 (2000).

[7]J. T. Vaughan, G. Adriany, M. Garwood, E. Yacoub, T. Duong, L. DelaBarre, P. Andersen, and K. Ugurbil, "Detunable transverse electromagnetic (TEM) volume coil for high-field NMR," Magn. Reson. Med. **47**(5), 990–1000 (2002).

[8]P. A. Bandettini, R. Bowtell, P. Jezzard, and R. Turner, "Ultrahigh field systems and applications at 7 T and beyond: Progress, pitfalls, and potential," Magn. Reson. Med. **67**(2), 317–321 (2012).

[9]D. I. Hoult and D. Phil, "Sensitivity and power deposition in a high-field imaging experiment," J. Magn. Reson. Imaging **12**(1), 46–67 (2000).

[10]F. Schick, "Whole-body MRI at high field: Technical limits and clinical potential," Eur. Radiol. **15**(5), 946–959 (2005).

[11]W. L. de Graaf, J. J. Zwanenburg, F. Visser, M. P. Wattjes, P. J. Pouwels, J. J. Geurts, C. H. Polman, F. Barkhof, P. R. Luijten, and J. A. Castelijns, "Lesion detection at seven Tesla in multiple sclerosis using magnetisation prepared 3D-FLAIR and 3D-DIR," Eur. Radiol. **22**(1), 221–231 (2012).

[12]B. Belaroussi, J. Milles, S. Carme, Y. M. Zhu, and H. Benoit-Cattin, "Intensity non-uniformity correction in MRI: Existing methods and their validation," Med. Image Anal. **10**(2), 234–246 (2006).

[13]U. Vovk, F. Pernus, and B. Likar, "A review of methods for correction of intensity inhomogeneity in MRI," IEEE Trans. Med. Imaging **26**(3), 405–421 (2007).

[14]H. P. Hetherington, N. I. Avdievich, A. M. Kuznetsov, and J. W. Pan, "RF shimming for spectroscopic localization in the human brain at 7 T," Magn. Reson. Med. **63**(1), 9–19 (2010).

[15]B. van den Bergen, C. A. Van den Berg, L. W. Bartels, and J. J. Lagendijk, "7 T body MRI: B1 shimming with simultaneous SAR reduction," Phys. Med. Biol. **52**(17), 5429–5441 (2007).

[16]C. Yang, W. Deng, and V. A. Stenger, "Simple analytical dual-band spectral-spatial RF pulses for B(1) + and susceptibility artifact reduction in gradient echo MRI," Magn. Reson. Med. **65**(2), 370–376 (2011).

[17]S. Orzada, S. Maderwald, B. A. Poser, A. K. Bitz, H. H. Quick, and M. E. Ladd, "RF excitation using time interleaved acquisition of modes (TIAMO) to address B1 inhomogeneity in high-field MRI," Magn. Reson. Med. **64**(2), 327–333 (2010).

[18]J. G. Sled, A. P. Zijdenbos, and A. C. Evans, "A nonparametric method for automatic correction of intensity nonuniformity in MRI data," IEEE Trans. Med. Imaging **17**(1), 87–97 (1998).

[19]D. W. Shattuck and R. M. Leahy, "BrainSuite: An automated cortical surface identification tool," Med. Image Anal. **6**(2), 129–142 (2002).

[20]D. W. Shattuck, S. R. Sandor-Leahy, K. A. Schaper, D. A. Rottenberg, and R. M. Leahy, "Magnetic resonance image tissue classification using a partial volume model," Neuroimage **13**(5), 856–876 (2001).

[21]J. Ashburner and K. J. Friston, "Voxel-based morphometry—The methods," Neuroimage **11**(6 Pt 1), 805–821 (2000).

[22]J. Ashburner, "Another MRI bias correction approach," in *8th International Conference on Functional Mapping of the Human Brain*, Japan, 2002.

[23]J. Ashburner and K. J. Friston, "Unified segmentation," Neuroimage **26**(3), 839–851 (2005).

[24]N. Weiskopf, A. Lutti, G. Helms, M. Novak, J. Ashburner, and C. Hutton, "Unified segmentation based correction of R1 brain maps for RF transmit field inhomogeneities (UNICORT)," Neuroimage **54**(3), 2116–2124 (2011).

[25]J. D. Gispert, S. Reig, J. Pascau, J. J. Vaquero, P. Garcia-Barreno, and M. Desco, "Method for bias field correction of brain T1-weighted magnetic resonance images minimizing segmentation error," Hum. Brain Mapp. **22**(2), 133–144 (2004).

[26]C. Hui, Y. X. Zhou, and P. Narayana, "Fast algorithm for calculation of inhomogeneity gradient in magnetic resonance imaging data," J. Magn. Reson. Imaging **32**(5), 1197–1208 (2010).

[27]J. B. Arnold, J. S. Liow, K. A. Schaper, J. J. Stern, J. G. Sled, D. W. Shattuck, A. J. Worth, M. S. Cohen, R. M. Leahy, J. C. Mazziotta, and D. A. Rottenberg, "Qualitative and quantitative evaluation of six algorithms for correcting intensity nonuniformity effects," Neuroimage **13**(5), 931–943 (2001).

[28]J. V. Manjón, J. J. Lull, J. Carbonell-Caballero, G. Garcia-Marti, L. Marti-Bonmati, and M. Robles, "A nonparametric MRI inhomogeneity correction method," Med. Image Anal. **11**(4), 336–345 (2007).

[29]R. G. Boyes, J. L. Gunter, C. Frost, A. L. Janke, T. Yeatman, D. L. Hill, M. A. Bernstein, P. M. Thompson, M. W. Weiner, N. Schuff, G. E. Alexander, R. J. Killiany, C. DeCarli, C. R. Jack, and N. C. Fox, "Intensity non-uniformity correction using N3 on 3-T scanners with multichannel phased array coils," Neuroimage **39**(4), 1752–1762 (2008).

[30]H. Mihara, N. Iriguchi, and S. Ueno, "A method of RF inhomogeneity correction in MR imaging," MAGMA (N.Y.) **7**(2), 115–120 (1998).

[31]C. Li, R. Huang, Z. Ding, C. Gatenby, D. Metaxas, and J. Gore, "A variational level set approach to segmentation and bias correction of images with intensity inhomogeneity," Med. Image Comput. Comput. Assist. Interv. **5242**, 1083–1091 (2008).

[32]P. A. Yushkevich, J. Piven, H. C. Hazlett, R. G. Smith, S. Ho, J. C. Gee, and G. Gerig, "User-guided 3D active contour segmentation of anatomical structures: Significantly improved efficiency and reliability," Neuroimage **31**(3), 1116–1128 (2006).

[33]W. Zheng, M. W. Chee, and V. Zagorodnov, "Improvement of brain segmentation accuracy by optimizing non-uniformity correction using N3," Neuroimage **48**(1), 73–83 (2009).

[34]F. Lusebrink, A. Wollrab, and O. Speck, "Cortical thickness determination of the human brain using high resolution 3T and 7T MRI data," Neuroimage **70**, 122–131 (2013).

[35]C. K. Kang, C. W. Park, J. Y. Han, S. H. Kim, C. A. Park, K. N. Kim, S. M. Hong, Y. B. Kim, K. H. Lee, and Z. H. Cho, "Imaging and analysis of lenticulostriate arteries using 7.0-Tesla magnetic resonance angiography," Magn. Reson. Med. **61**(1), 136–144 (2009).

[36]C. von Morze, D. Xu, D. D. Purcell, C. P. Hess, P. Mukherjee, D. Saloner, D. A. Kelley, and D. B. Vigneron, "Intracranial time-of-flight MR angiography at 7T with comparison to 3T," J. Magn. Reson. Imaging **26**(4), 900–904 (2007).

[37]K. Setsompop, V. Alagappan, A. C. Zelinski, A. Potthast, U. Fontius, F. Hebrank, F. Schmitt, L. L. Wald, and E. Adalsteinsson, "High-flip-angle slice-selective parallel RF transmission with 8 channels at 7 T," J. Magn. Reson. **195**(1), 76–84 (2008).

[38]P. F. Van de Moortele, E. J. Auerbach, C. Olman, E. Yacoub, K. Ugurbil, and S. Moeller, "T1 weighted brain images at 7 Tesla unbiased for Proton Density, T2* contrast and RF coil receive B1 sensitivity with simultaneous vessel visualization," Neuroimage **46**(2), 432–446 (2009).

[39]D. W. McRobbie, *MRI from Picture to Proton*, 2nd ed. (Cambridge University Press, Cambridge, UK, 2007).

[40]M. Sasaki, T. Inoue, K. Tohyama, H. Oikawa, S. Ehara, and A. Ogawa, "High-field MRI of the central nervous system: Current approaches to clinical and microscopic imaging," Magn. Reson. Med. Sci. **2**(3), 133–139 (2003).